Observations of the missing baryons in the warm–hot intergalactic medium

F. Nicastro[1,2]*, J. Kaastra[3], Y. Krongold[4], S. Borgani[5,6,7], E. Branchini[8], R. Cen[9], M. Dadina[10], C. W. Danforth[11], M. Elvis[2], F. Fiore[1], A. Gupta[12], S. Mathur[13], D. Mayya[14], F. Paerels[15], L. Piro[16], D. Rosa-Gonzalez[14], J. Schaye[17], J. M. Shull[11], J. Torres-Zafra[18], N. Wijers[17] & L. Zappacosta[1]

It has been known for decades that the observed number of baryons in the local Universe falls about 30–40 per cent short[1,2] of the total number of baryons predicted[3] by Big Bang nucleosynthesis, as inferred[4,5] from density fluctuations of the cosmic microwave background and seen during the first 2–3 billion years of the Universe in the so-called 'Lyman α forest'[6,7] (a dense series of intervening H I Lyman α absorption lines in the optical spectra of background quasars). A theoretical solution to this paradox locates the missing baryons in the hot and tenuous filamentary gas between galaxies, known as the warm–hot intergalactic medium. However, it is difficult to detect them there because the largest by far constituent of this gas—hydrogen—is mostly ionized and therefore almost invisible in far-ultraviolet spectra with typical signal-to-noise ratios[8,9]. Indeed, despite large observational efforts, only a few marginal claims of detection have been made so far[2,10]. Here we report observations of two absorbers of highly ionized oxygen (O VII) in the high-signal-to-noise-ratio X-ray spectrum of a quasar at a redshift higher than 0.4. These absorbers show no variability over a two-year timescale and have no associated cold absorption, making the assumption that they originate from the quasar's intrinsic outflow or the host galaxy's interstellar medium implausible. The O VII systems lie in regions characterized by large (four times larger than average[11]) galaxy overdensities and their number (down to the sensitivity threshold of our data) agrees well with numerical simulation predictions for the long-sought warm–hot intergalactic medium. We conclude that the missing baryons have been found.

Numerical simulations in the framework of the commonly accepted (ΛCDM) cosmological paradigm predict that, starting at a redshift of $z \approx 2$ and during the continuous process of structure formation, diffuse baryons in the intergalactic medium (IGM) condense into a filamentary web (with electron densities of $n_e \approx 10^{-6}$–10^{-4} cm^{-3}) and undergo shocks that heat them up to temperatures of $T \approx 10^5$–10^7 K, making the by-far-largest constituent of the IGM, hydrogen, mostly ionized[8,9]. At the same time, galactic outflows powered by stellar and active galactic nucleus (AGN) feedback enrich the IGM baryons with metals[12]. How far from galaxies these metals roam depends on the energetics of these winds, but it is expected that metals and galaxies are spatially correlated.

This shock-heated, metal-enriched medium, known as the warm–hot intergalactic medium (WHIM), is made up of three observationally distinct phases: (1) a warm phase, with $T \approx 10^5$–$10^{5.7}$ K, where neutral hydrogen is still present with an ion fraction of $f_{HI} > 10^{-6}$, and the best observable metal ion tracers are O VI (with main transitions in the far ultraviolet; FUV) and C V (with transitions in the soft X-rays); (2) a hot phase with $T \approx 10^{5.7}$–$10^{6.3}$ K, where $f_{HI} \approx 10^{-6}$–10^{-7}, and O VII (with

transitions in the soft X-rays) largely dominates metals with ion fractions near unity; and (3) an even hotter phase ($T \approx 10^{6.3}$–10^7 K), coinciding with the outskirts of massive virialized groups and clusters of galaxies, where H I and H-like metals are present only in traces[9]. The warm phase of the WHIM has indeed been detected and studied in detail in the past few years and is estimated to contain an additional 15^{+8}_{-4}% fraction of the baryons (for example, see refs [1,2] and references therein; Table 1). This brings the total detected fraction to 61^{+14}_{-12}%, but still leaves us with a large (39^{+12}_{-14}%) fraction of elusive baryons, which—if theory is correct—should be searched for in the hotter phases of the WHIM. In particular, the diffuse phase at $T \approx 10^{5.7}$–$10^{6.3}$ K should contain the vast majority of the remaining WHIM baryons, and it is traced by O VII. Optimal signposts for this WHIM phase are then the O VII Heα absorption lines; however, these are predicted to be relatively narrow (with a Doppler parameter thermal component $b_{th}(O) \approx 20$–46 km s^{-1}), extremely shallow (rest-frame equivalent widths, EW ≲ 10 mÅ) and rare[8,9]. Such lines are unresolved by current X-ray spectrometers and need a signal-to-noise ratio per resolution element greater than or equal to ∼20 in the continuum to be detected at a single-line statistical significance (that is, before accounting for redshift trials; see Methods) exceeding ∼3σ. This requires multi-million-second exposures against the brightest possible targets that are available at sufficiently high redshift ($z \gtrsim 0.3$).

Here we report on the longest observation performed with the X-ray multi-mirror mission (XMM)-Newton reflection grating spectrometer (RGS) on a single continuum target, the brightest X-ray blazar 1ES 1553+113, with $z > 0.4$ (see Methods). The quality of this RGS spectrum makes it a goldmine for X-ray absorption-line studies (see Methods and Extended Data Figs. 1 and 2). We detect a number of unresolved absorption lines in both RGS units (RGS1 and RGS2) and at single-line statistical significance exceeding 2.7σ–3σ. (Throughout the paper, we report ranges of statistical significance, where the upper boundary is the actual measured single-line statistical

Table 1 | Cosmic baryon census at $z < 0.5$

|	$\Omega_b h^2$	$\Omega_b / \Omega_b^{Plank}$
Stars in galaxies	0.0015 ± 0.0004	(7 ± 2)%
Cold gas in galaxies	0.00037 ± 0.00009	(1.7 ± 0.4)%
Galaxies' hot disks/haloes	0.0011 ± 0.0007	(5 ± 3)%
Hot ICM	0.00088 ± 0.00033	(4.0 ± 1.5)%
Photoionized Lyman α forest	0.0062 ± 0.0024	(28 ± 11)%
WHIM with 10^5 K $\leq T < 10^{5.7}$ K	$0.0033^{+0.0018}_{-0.0009}$	15^{+8}_{-4}%
WHIM with $10^{5.7}$ K $\leq T < 10^{6.2}$ K	>0.002 and <0.009	>9% and <40%
Total	>0.013 and < 0.026	>59% and <118%

Ω_b, baryon density; Ω_b^{Plank}, total baryon density measured by the Planck satellite.

[1]Istituto Nazionale di Astrofisica (INAF), Osservatorio Astronomico di Roma, Rome, Italy. [2]Harvard–Smithsonian Center for Astrophysics, Cambridge, MA, USA. [3]SRON Netherlands Institute for Space Research, Utrecht, The Netherlands. [4]Instituto de Astronomia Universidad Nacional Autonoma de Mexico, Mexico City, Mexico. [5]Physics Department, University of Trieste, Trieste, Italy. [6]INAF—Osservatorio Astronomico di Trieste, Trieste, Italy. [7]Istituto Nazionale di Fisica Nucleare (INFN)—Sezione di Trieste, Trieste, Italy. [8]Physics Department, University of Roma Tre, Rome, Italy. [9]Department of Astrophysical Science, Princeton University, Princeton, NJ, USA. [10]INAF—Osservatorio di Astrofisica e Scienza dello Spazio di Bologna, Bologna, Italy. [11]Department of Astrophysical Science, University of Colorado, Boulder, CO, USA. [12]Columbus State Community College, Columbus, OH, USA. [13]Ohio State University, Columbus, OH, USA. [14]Instituto Nacional de Astrofísica, Óptica y Electrónica, Puebla, Mexico. [15]Department of Astronomy, Columbia University, New York, NY, USA. [16]INAF - Istituto di Astrofisica e Planetologia Spaziali, Rome, Italy. [17]Leiden Observatory, Leiden, The Netherlands. [18]Instituto de Astrofísica de La Plata (IALP-UNLP), La Plata, Argentina. *e-mail: fabrizio.nicastro@oa-roma.inaf.it
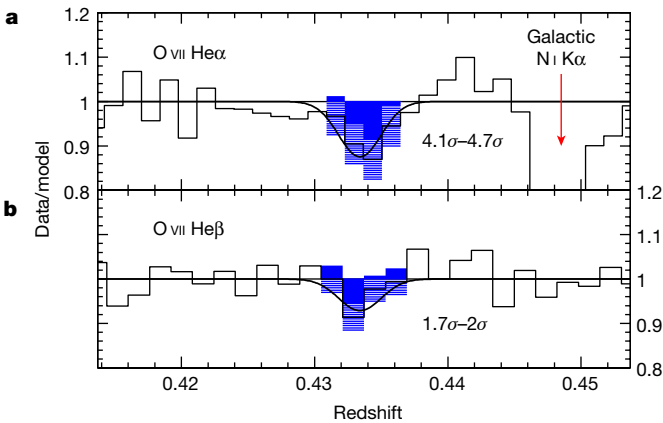
Fig. 1 | Intervening absorber at $z_1^X = 0.4339 \pm 0.0008$. a, b, Ratios of XMM-Newton RGS1 and RGS2 spectra of the blazar 1ES 1553+113 with their local best-fitting continuum model, showing the two O VII Heα (**a**) and Heβ (**b**) absorption lines that identify System 1 at a 'true' statistical significance of 3.9σ–4.5σ (these statistical significance boundaries correspond to Gaussian probabilities of chance detection of $P = 4.8 \times 10^{-5}$ and $P = 3.4 \times 10^{-6}$, respectively). Shaded blue regions indicate the lines detected in the X-ray region. Hatched blue intervals in the line histograms represent ±1σ errors (statistical plus 2% systematic errors). Black curves are best-fitting Gaussians folded through the instrumental RGS line spread function.

significance, whereas the lower boundary is the measured significance, conservatively corrected for observed systematic errors in the RGS spectrum; see Methods and Extended Data Fig. 3). Particularly, two of these lines are seen at significances of 4.1σ–4.7σ (Figs. 1a) and 3.7σ–4.2σ (Fig. 2b) at wavelengths where no Galactic absorption is expected and no instrumental feature is present (Extended Data Fig. 2;
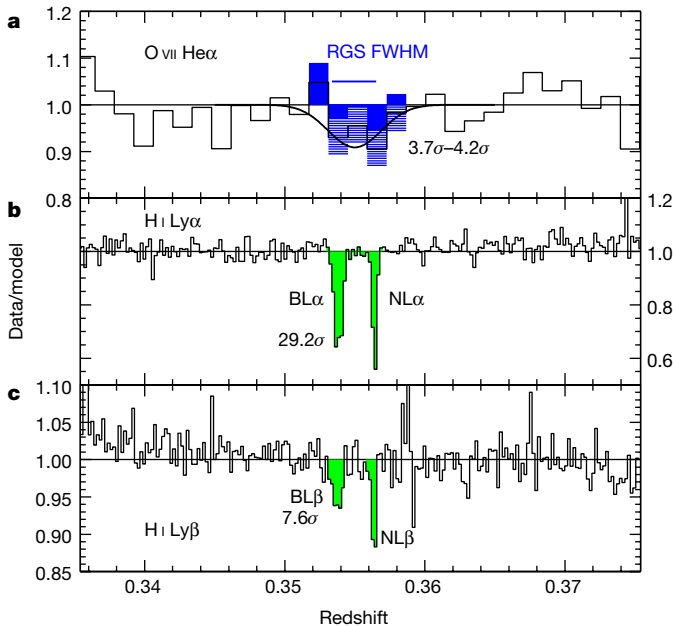
Fig. 2 | Intervening absorber at $z_2^X = 0.3551^{+0.0003}_{-0.0015}$. a–c, Same as Fig. 1, but showing the results for an O VII Heα absorber (**a**) and two H I Lyα (**b**) and Lyβ (**c**) absorbers only ~750 km s⁻¹ apart and both at redshifts consistent with the X-ray System 2. The X-ray absorber has a 'true' statistical significance of 2.9σ–3.7σ; these statistical significance boundaries correspond to Gaussian probabilities of chance detection of $P = 1.9 \times 10^{-3}$ and $P = 10^{-4}$, respectively). Neither of the two H I absorbers in **b** and **c** can be physically associated to the O VII Heα absorber (**a**), implying the presence of at least three co-located—but dramatically different physically— gaseous phases.
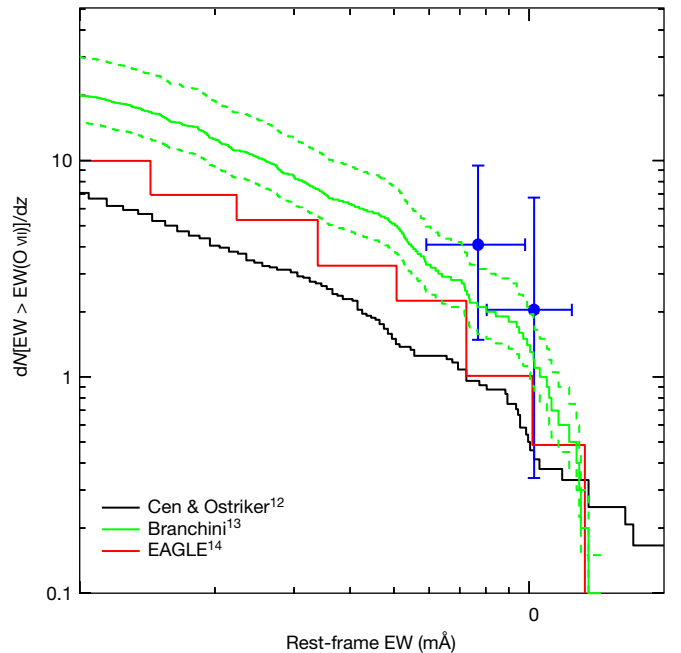
**Fig. 3 | Agreement between data and predictions.** Cumulative number density, N, of O VII Heα intergalactic absorbers per unit redshift, z, with an EW greater than a given threshold, versus the rest-frame EW threshold. The lines show different predictions[12–14], compared with the two data points (blue points) that correspond to our two detections at $z_1^X = 0.3551$ and $z_2^X = 0.4339$. All error bars correspond to 1σ and vertical error bars are computed using low-number Poisson statistics. The black curve shows predictions from simulations performed with galactic super-winds and without imposing local thermodynamic equilibrium[12]. The green curve corresponds to a range of predictions from ref. [13]. The red line shows EAGLE (Evolution and Assembly of Galaxies and their Environments) results for the 100 Mpc reference simulation of ref. [14] at $z = 0.1$, and an O VII Heα Doppler parameter $b = 100$ km s⁻¹ is used in the conversion from column density to EW.

see Methods). We attribute these lines to intervening O VII Heα absorbers at redshifts of $z_1^X = 0.4339 \pm 0.0008$ (hereafter, System 1) and $z_2^X = 0.3551^{+0.0003}_{-0.0015}$ (System 2) (Extended Data Table 1). Their statistical significances decrease to 3.5σ–4σ and 2.9σ–3.7σ, respectively, after accounting for the number of redshift trials (see Methods). Interestingly, a lower-significance (1.7σ–2σ) absorption line can be modelled at the wavelength where the O VII Heβ line for System 1 is expected (Fig. 1b, Extended Data Figs. 1, 2), which increases the 'true' statistical significance of System 1 to 3.9σ–4.5σ (see Methods).

Given the proximity of our two systems with the upper limit $z \lesssim 0.48$ that we estimate for the redshift of our target (see Methods), we cannot rule out that these two systems are imprinted by material intrinsic to the blazar environment that outflows from this environment at speeds lower than 0.05c–0.12c, where c is the speed of light. However, a number of reasons make this scenario implausible (see Methods, Extended Data Fig. 4 and Extended Data Table 2 for details). The identification of System 1 and System 2 as genuine WHIM/circumgalactic medium (CGM) systems seems much more reasonable.

By modelling the X-ray data with our hybrid-ionization models (see Methods), we estimate the temperatures (T^X) and the oxygen (N_O^X) and equivalent H (N_H^X; modulo metallicity) column densities for System 1 and System 2. We obtain $T_1^X = (6.8^{+9.6}_{-3.6}) \times 10^5$ K, $N_{O,1}^X = (7.8^{+3.9}_{-2.4}) \times 10^{15}$, $N_{H,1}^X = (1.6^{+0.8}_{-0.5})(Z/Z_\odot)^{-1} \times 10^{19}$ cm⁻² for System 1 and $T_2^X = (5.4^{+9.0}_{-1.7}) \times 10^5$ K, $N_{O,2}^X = (4.4^{+2.4}_{-2.0}) \times 10^{15}$ and $N_{H,2}^X = (0.9^{+0.5}_{-0.4})(Z/Z_\odot)^{-1} \times 10^{19}$ cm⁻² for System 2, where Z is the metallicity and $Z_\odot$ denotes the metallicity of the Sun.

For both systems, these quantities are in good agreement with predictions for the hot phase of the WHIM[8,9,12]. Moreover, the number of
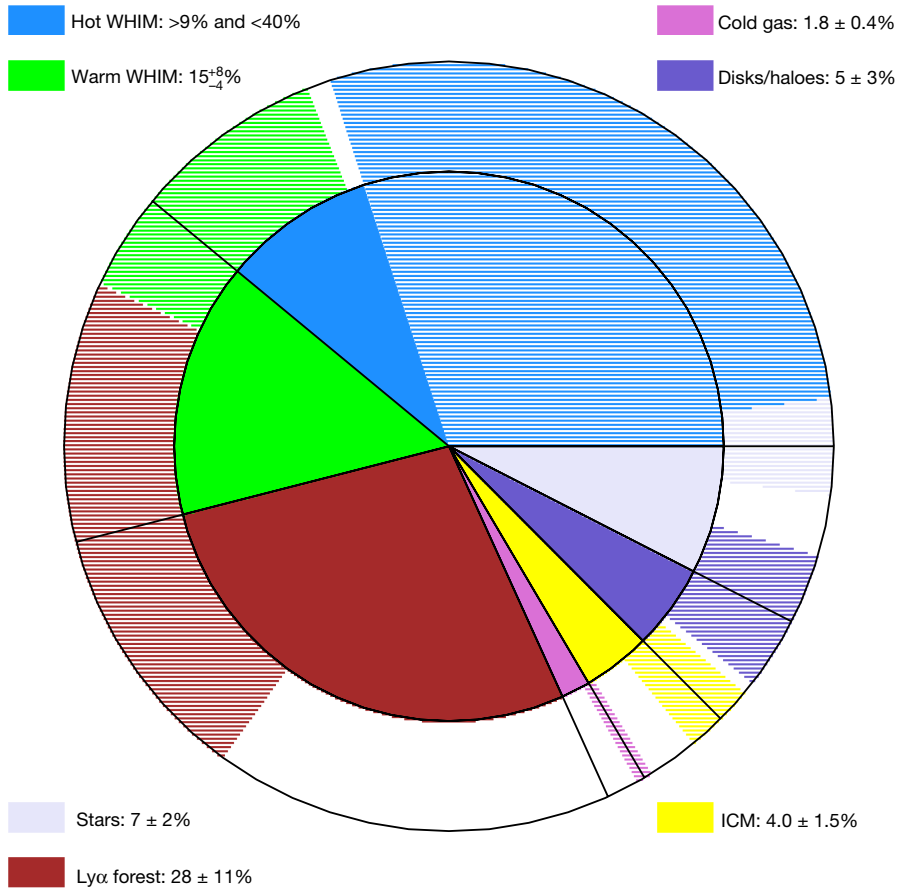
Fig. 4 | Updated baryon census. Pie diagram of the baryonic components of the local universe. Hatched regions in the external corona indicate the 90% uncertainties on the individual components; they are plotted across one of the two sides of each slice to show to what extent of each slice could be smaller or bigger. The exception is our measurement of the $10^{5.7}$ K $\leq T \leq 10^{6.2}$ K WHIM component, where the solid-shaded area shows the 3σ lower limit on the amount of baryons in these physical conditions, whereas the hatched area indicates and represents our 3σ upper limit, namely, the maximum amount of baryons that is allowed by our study to be contained in this phase at 99.97% confidence (see also Table 1).

detected O VII absorbers is consistent with predictions from a number of models[8,13,14] (Fig. 3).

The identification of the WHIM systems 1 and 2 is also supported by three independent pieces of evidence (see Methods for details): (1) significant galaxy overdensities at the locations of the two absorbers (Extended Data Figs. 5–7); (2) for System 1, the compatibility (at 2.3σ level) between the spectrum of 1ES 1553+113 obtained with the Hubble Space Telescope's cosmic origins spectrograph (HST-COS) and the presence of a very broad and shallow (and so physically consistent with O VII) H I Lyα absorber at the redshift of the X-ray absorber; (3) for System 2, the presence of two strong (but physically inconsistent with O VII) intervening hydrogen absorbers only 750 km s^{-1} apart, and at redshifts consistent with that of the X-ray absorber (Fig. 2b, c).

Neither of the two strong H I absorbers seen in the HST-COS spectrum at redshifts consistent with that of System 2 (Fig. 2b) are sufficiently hot to produce the amount of O VII absorption seen in the X-rays (see Methods). This must be produced by even hotter gas (as indicated by X-ray data fitting), possibly confined between the two colder H I phases, that gives rise to undetectable broad H I Lyα absorption. For both X-ray absorbers, we use the HST-COS spectrum to derive 3σ upper limits on the column densities of H I and O VI (see Methods).

For System 1 we obtain $N_{\mathrm{HI,1}}^{\mathrm{FUV}} < 3.9 \times 10^{13}$ cm^{-2} and $N_{\mathrm{OVI,1}}^{\mathrm{FUV}} < 3.2 \times 10^{13}$ cm^{-2}, and for System 2 we get $N_{\mathrm{HI,2}}^{\mathrm{FUV}} < 3.5 \times 10^{13}$ cm^{-2} and $N_{\mathrm{OVI,2}}^{\mathrm{FUV}} < 8.1 \times 10^{13}$ cm^{-2}. Comparing $N_{\mathrm{OVI}}^{\mathrm{FUV}}$ with the 1σ lower boundary on $N_{\mathrm{O}}^{\mathrm{X}}$ allows us to constrain the minimum ionization correction needed (see Methods) and so to further limit the temperatures of the two systems in the intervals $T_1^{\mathrm{X}} = (0.8-1.6) \times 10^6$ K

and $T_2^{\mathrm{X}} = (0.5-1.4) \times 10^6$ K. Correcting the 3σ upper limits on $N_{\mathrm{HI}}^{\mathrm{FUV}}$ for the central values of the H I ionization fractions gives upper limits on the total H column densities of the two systems of $N_{\mathrm{H,1}}^{\mathrm{FUV}} < 1.4 \times 10^{20}$ cm^{-2} and $N_{\mathrm{H,2}}^{\mathrm{FUV}} < 9 \times 10^{19}$ cm^{-2}, respectively. Finally, comparing these columns with those obtained from the X-ray data, $N_{\mathrm{H}}^{\mathrm{X}}$, we derive 3σ lower limits on the metallicity of the systems, $Z_1^{\mathrm{X}} > 0.1 Z_\odot$ and $Z_2^{\mathrm{X}} > 0.1 Z_\odot$ (Extended Data Table 3).

For both systems we assume as upper limit on the average WHIM metallicity (see Methods) the value $Z_{\mathrm{ICM}} = 0.2 Z_\odot$ found in the peripheries (at r_{500}; namely, the distance from the centre of the cluster where the density of the intra-cluster medium is 500 times the average density of the Universe.) of the intra-cluster medium[15]. With metallicity constrained in the $Z \approx 0.1 Z_\odot - 0.2 Z_\odot$ interval, we can now use the 68% confidence intervals on the equivalent H column densities to constrain the cosmological mass density of baryons with temperatures in the interval $T \approx 10^{5.7} - 10^{6.2}$ K. By parameterizing the lower limit by the inverse of the metallicity in units of $0.2 Z_\odot$, we obtain a baryon density Ω_{b} of $0.002(Z_{0.2})^{-1} < \Omega_{\mathrm{b}}^{10^{5.7}\mathrm{K} \leq T \leq 10^{6.2}\mathrm{K}} h^2 < 0.009$, corresponding to $9(Z_{0.2})^{-1}-40\%$ of the total baryon density measured by the Planck satellite[4], in good agreement with predictions[8,9] and potentially sufficient to complete the baryon census (Fig. 4, Table 1).

Finally, theory predicts that metal-enriched WHIM absorbers should lie in the proximity of galaxy overdensities, either in the CGM of a particular galaxy or in the more diffuse IGM. Consistent with expectations, our photometric redshifts of the $r' > 23.5$ galaxies in the $30' \times 30'$ field surrounding 1ES 1553+113 indicate that both WHIM systems 1 and 2 are found in regions of substantial galaxy overdensities (Extended

Data Figs. 5–7; see Methods). For System 1 we have a number of spectroscopic redshift confirmations (that is, within ±900 km s^{-1} of the absorber; see Methods) showing in particular the presence of a bright (Sloan Digital Sky Survey magnitude, $i' = 19.6$) spiral at only 129 kpc and -15 km s^{-1} from the absorber. For System 2, the only spectroscopically confirmed galaxy (out of only four spectroscopic redshifts available), a bright $i' = 20.5$ elliptical, lies far (633 kpc and $+370$ km s^{-1}) from the absorber. This may explain the different baryon column densities of the two systems: System 1, with its higher column density, could be imprinted by the CGM of the nearby spiral, whereas System 2, with its lower baryon column density, could be produced by a more extended diffuse IGM filament connecting a structure of galaxies.

Online content

Any Methods, including any statements of data availability and Nature Research reporting summaries, along with any additional references and Source Data files, are available in the online version of the paper at https://doi.org/10.1038/s41586-018-0204-1.

1. Shull, J. M., Smith, B. D. & Danforth, C. W. The baryon census in a multiphase intergalactic medium: 30% of the baryons may still be missing. *Astrophys. J.* **759**, 23 (2012).
2. Nicastro, F., Krongold, Y., Mathur, S. & Elvis, M. A decade of warm hot intergalactic medium searches: where do we stand and where do we go? *Astron. Nachr.* **338**, 281–286 (2017).
3. Kirkman, D., Tytler, D., Suzuki, N., O'Meara, J. M. & Lubin, D. The cosmological baryon density from the deuterium-to-hydrogen ratio in QSO absorption systems: D/H toward Q1243+3047. *Astrophys. J. Suppl. Ser.* **149**, 1–28 (2003).
4. Planck Collaboration. Planck 2015 results. XIII. Cosmological parameters. *Astron. Astrophys.* **594**, A13 (2016).
5. Komatsu, E. et al. Five-year Wilkinson microwave anisotropy probe observations: cosmological interpretation. *Astrophys. J. Suppl. Ser.* **180**, 330–376 (2009).
6. Rauch, M. The Lyman alpha forest in the spectra of QSOs. *Annu. Rev. Astron. Astrophys.* **36**, 267–316 (1998).
7. Weinberg, D. H., Miralda-Escudé, J., Hernquist, L. & Katz, N. A lower bound on the cosmic baryon density. *Astrophys. J.* **490**, 564–570 (1997).
8. Cen, R. & Ostriker, J. P. Where are the baryons? *Astrophys. J.* **514**, 1–6 (1999).
9. Davé, R. et al. Baryons in the warm–hot intergalactic medium. *Astrophys. J.* **552**, 473–483 (2001).
10. Bonamente, M. et al. A possible Chandra and Hubble Space Telescope detection of extragalactic WHIM towards PG 1116+215. *Mon. Not. R. Astron. Soc.* **457**, 4236–4247 (2016).
11. Willmer, C. N. A. et al. The deep evolutionary exploratory probe 2 galaxy redshift survey: the galaxy luminosity function to z~1. *Astrophys. J.* **647**, 853–873 (2006).
12. Cen, R. & Ostriker, J. P. Where are the baryons? II. Feedback effects. *Astrophys. J.* **650**, 560–572 (2006).
13. Branchini, E. et al. Studying the warm hot intergalactic medium with gamma-ray bursts. *Astrophys. J.* **697**, 328–344 (2009).
14. Schaye, J. et al. The EAGLE project: simulating the evolution and assembly of galaxies and their environments. *Mon. Not. R. Astron. Soc.* **446**, 521–554 (2015).
15. Mernier, F. et al. Radial metal abundance profiles in the intra-cluster medium of cool-core galaxy clusters, groups, and ellipticals. *Astron. Astrophys.* **603**, A80 (2017).

Author contributions F.N. designed the study (together with J.K., L.P., S.B., L.Z., S.M., M.E., R.C., F.P. and A.G.), reduced and analysed the X-ray data, analysed the FUV data, extracted diagnostics by modelling the X-ray and FUV data and wrote the paper. Y.K., J.K., L.P., S.M., M.E., F.P., F.F. and A.G. helped with the analysis and modelling of the X-ray spectra. M.D. and F.N. designed and executed the Monte Carlo simulations used to evaluate the statistical significance of the absorbers. J.K. provided the most up-to-date XMM-Newton RGS calibrations and effective area corrections. C.W.D. and J.M.S. reduced the HST-COS data, extracted the G130 and G160 final spectra and helped with the interpretation of those spectra. Y.K. performed the optical photometric observations, as well as the reduction and analysis of those data, with the help of D.M. and D.R.-G. D.R.-G. and J.T.Z. provided the galaxies' spectroscopic redshifts. S.B., E.B., J.S., N.W. and R.C. provided hydrodynamical simulations and general theoretical support to the results. In particular, J.S. and N.W. provided results from high-resolution Eagle simulations and F.P. helped to extract the number density of O VII absorbers from these simulations. All authors contributed equally to the discussion of the results and commented on the manuscript.

METHODS

Errors. Throughout the paper, uncertainties are quoted at 68% significance, unless stated otherwise.

Redshift of 1ES 1553+113. The exact redshift of this blazar is unknown, but a tight spectroscopic lower limit of $z > 0.413$ is imposed by the detection up to this redshift (and close to the long-wavelength end of the HST-COS bandpass) of intervening H I Lyα absorption in the HST-COS spectrum of this target. Based on the lack of secure H I Lyα detections at $z > 0.413$, the frequency of the H I Lyα absorbers (about one every 10 Å, down to the sensitivity of the regions of the HST-COS spectrum with the highest signal-to-noise ratio) and the decreasing signal-to-noise ratio of the HST-COS spectrum at $\lambda > 1,750$ Å, we estimate a conservative upper limit of $z \lesssim 0.48$. More recently, a $z = 0.49 \pm 0.04$ redshift estimate has been set based on γ-ray observations of extragalactic background light absorption[16], consistent with our spectroscopic estimates.

Statistical significance. We define the 'single-line statistical significance' of an absorption line as the ratio $EW/\Delta(EW)$ between the line equivalent width and its negative 1σ error (but see 'Additional systematic errors in the RGS spectrum of 1ES 1553+113' for a correction for effective-area systematic errors in the RGS spectrum). For a blind search of intervening absorbers, this is not the actual statistical significance of the line, unless a prior is used for the absorber redshift. In the absence of such a prior, we estimate the 'true' statistical significance of a given line by performing Monte Carlo simulations. Each simulation consists of: (a) producing 18 RGS1 and RGS2 mock spectra with the same exposures and continuum best-fitting parameters of our 18 XMM-Newton observations, (b) co-adding them and (c) fitting the co-added spectra (for RGS1 and RGS2) with a continuum model plus an unresolved and negative-only Gaussian, whose position is allowed to vary from the rest-frame position of the transition and its redshifted position at $z = 0.5$ (this redshift is conservatively assumed to be the blazar redshift; also, for O VII Heα lines, it coincides with the long-wavelength end of the RGSs). We repeat this procedure 10,000 times and evaluate the chance of detection of a line with single-line statistical significance greater than a given threshold.

We adopt this 'true' statistical significance for the X-ray line with the highest single-line statistical significance and use that line as a prior for other associated X-ray lines, when present. Finally, we evaluate the statistical significance of an X-ray absorption system by adding in quadrature the 'true' statistical significances of the lines of the system.

XMM-Newton RGS spectra of 1ES 1553+113. XMM-Newton observed 1ES 1553+113 for two consecutive cycles and for a total observing time of 1.75 Ms under a cycle-14 Very Large Program. Specifically, observations were made for 0.8 Ms between 29 July 2015 and 5 September 2015 (Epoch 1; black line in Extended Data Fig. 4a, b) and for 0.95 Ms between 1 February 2017 and 22 February 2017 (Epoch 2; red line in Extended Data Fig. 4a, b). Four short additional observations performed between 6 September 2001 and 28 July 2014 were also present in the archive, totalling an observing time of 0.096 Ms. We reduced these observations with the latest version (16.1.0) of the XMM-Newton Science Analysis System (SAS) software and current calibration files and extracted the RGS (RGS1 and RGS2) spectra and responses by applying the latest calibration corrections. We used the most up-to-date effective area corrections by switching on the parameters *withrectification* and *witheffectiveareacorrection* of the SAS tool *rgsrgsrmfge* that generates the RGS response matrices. The second of these parameters, in particular, eliminates some residual wiggle seen in the spectra of the calibration targets Mkn 421 and PKS 2155-304 at wavelength ~29−32 Å (Extended Data Fig. 2). We also added a 2% systematic uncertainty to the RGS counts, as estimated by the team of RGS calibrators, led by J.K. The final, cleaned RGS spectra have an exposure time of 1.85 Ms and are shown in Extended Data Fig. 1.

The RGS spectrum of 1ES 1553+113 has a signal-to-noise ratio per resolution element of SNRE = 33 at $\lambda = 23.5−30.2$ Å, and SNRE = 23 at $\lambda = 21.6−23.5$ Å (where only one of the two RGSs is present) and $\lambda = 30.2−32$ Å (the long-wavelength end of the RGS bandpass). This implies a 90% sensitivity of EW ≥ 3.5 mÅ and EW ≥ 4.5 mÅ to intervening O VII Heα lines in the two redshift intervals $0.08 \leq z \leq 0.4$ and $z \in [(0, 0.08) \cup (0.4, 0.5)]$, respectively. The 8−33 Å RGS spectrum shows a number of narrow (unresolved) line-like negative features (Extended Data Fig. 1), eight of which are identifiable with Galactic absorption (marked and labelled in blue in Extended Data Fig. 1): Ne X Lyα ($\lambda = 12.131 \pm 0.035$ Å), Ne IX Heα ($\lambda = 13.460 \pm 0.035$ Å), O VII Heα ($\lambda = 21.586 \pm 0.035$ Å), O IV Kα + O I Kγ ($\lambda = 22.701 \pm 0.035$ Å), O II Kα ($\lambda = 23.339 \pm 0.035$ Å), O I Kα ($\lambda = 23.512 \pm 0.035$ Å), N VI Kα ($\lambda = 28.772 \pm 0.035$ Å) and N I Kα ($\lambda = 31.281 \pm 0.035$ Å), where half of the RGS full-width at half-maximum (FWHM) resolution element is used as position error. Two additional unresolved absorption lines are detected in both RGSs at combined single-line statistical significances of $4.1\sigma−4.7\sigma$ (Fig. 1a, Extended Data Figs. 1, 2 and Extended Data Table 1) and $3.7\sigma−4.2\sigma$ (Fig. 2a, Extended Data Figs. 1, 2 and Extended Data Table 1), at wavelengths where (1) no Galactic absorption is expected and (2) neither of the two spectrometers is affected by instrumental features due to cool

pixels in the dispersing detector (Extended Data Fig. 2). These are the lines here identified as intervening WHIM O VII Heα at $z_1^X = 0.4339 \pm 0.0008$ (System 1) and $z_2^X = 0.3551^{+0.0003}_{-0.0015}$ (System 2; Extended Data Table 1 and Figs. 1, 2). An additional lower-significance ($1.7\sigma−2\sigma$) line is detected at a $\lambda = 26.69 \pm 0.09$ Å and is identifiable as O VII Heβ at a redshift consistent with z_1^X (Fig. 1b, Extended Data Figs. 1, 2, and Extended Data Table 1).

Additional systematic errors in the RGS spectrum of 1ES 1553+113. In addition to the 2% systematic error estimated by the team of RGS calibrators for any RGS spectrum, we look for the presence of any systematic errors specific to our co-added 1.85-Ms RGS spectra of 1ES 1553+113, by performing the following Monte Carlo test. We re-fit the RGS spectra of 1ES 1553+113 by adding to the best-fitting continuum-plus-absorption-line models shown in Extended Data Fig. 1 an unresolved Gaussian (whose normalization is allowed to be either positive or negative) at a random position in the $\lambda = 8−33$ Å range. We then evaluate the single-line statistical significance of the line (assumed to be negative for emission lines and positive for absorption lines). There are about 400 RGS resolution elements in this wavelength range, and we therefore repeat this operation 1,000 times. Extended Data Fig. 3 shows the distribution of measured single-line significances (black histogram) and compares it with the expected distribution for a normal distribution with standard deviation of unity (red curve). The data distribution is symmetric (indicating that any systematic errors are also acting symmetrically) but slightly flatter than the red curve in Extended Data Fig. 3. We think that this is due to uncertainties in the RGS effective areas at wavelengths corresponding to cool pixels in the dispersing detectors. This effect can indeed be seen in Extended Data Fig. 2, where the residual excesses or deficits of counts in the data at, for example, $\lambda \approx 27.7$ Å, 30.2−3.3 Å and 31.1−31.2 Å, all correspond to strong effective-area instrumental features (red and black curves). The normal distribution that best fits our Monte Carlo results has a standard deviation of 1.15 (green curve in Extended Data Fig. 3), which should then be used to correct the statistical significance of lines detected at wavelengths affected by cool pixels. The absorption lines reported here are all found in relatively clean effective-area spectral regions. However, to be conservative, for each line we use a range of statistical significances, whose lower and upper boundaries are the measured single-line statistical significances corrected for effective-area-induced systematic errors and the actual single-line significance, respectively. Such single-line statistical significance intervals are then propagated to 'true' statistical significance intervals by allowing for redshift trials, as detailed above.

X-ray diagnostics: temperature and baryon column density. We use our hybrid-ionization models (that is, models of collisionally ionized gas perturbed by photoionization, at a given redshift, by the meta-galactic radiation field)[17], to characterize the temperature T^X and the equivalent H column density N_H^X(modulo the absorber's absolute metallicity) of the X-ray absorbers. In our models we use relative metallicities from ref. [18]. Our spectral WHIM models include more than 3,000 line transitions in the soft X-ray band (energies $E \approx 0.1−2$ keV). For each transition, the line optical depth and Voigt profile are self-consistently computed for pairs of values of the gas temperature (that is, ionization structure) and equivalent H column density, which are let free to vary in the fit. At typical WHIM conditions, the temperature of these models is well constrained by the detected ion transitions, as well as by the upper limits that can be set on the presence of lower- or higher-ionization ion transitions. For example, in the 8−33 Å band covered by the RGSs and at the temperature where O VII is the dominant ion of oxygen, the low-T boundary is mostly set by the non-detection of K-shell transitions of O IV−O VI and M-shell transitions of Fe VII−Fe XVI, whereas the high-T boundary is set by the absence of the K-shell transitions of O VIII and Ne IX−Ne X and the L-shell transitions of Fe XVII−Fe XXIV.

We note that our temperature estimates depend on our assumption of gas in collisional ionization equilibrium, perturbed by the meta-galactic ionizing radiation field. This assumption may not be valid in particularly low-density regions, where the post-shock electron–ion relaxation timescale is longer than the Hubble time[19], and could lead to an overestimation of the actual electron temperature[19]. However, even for a difference by a factor of 2 in electron temperature, the fraction of our tracer ion, O VII, at its peak temperature interval, $T \approx 5 \times 10^5−2 \times 10^6$ K, is not considerably affected by this effect (see, for example, Fig. 4 of ref. [19]). This makes our oxygen column density estimates virtually independent of the exact ionization state of the gas.

The EWs of the detected O VII lines, together with the limits on the EWs of higher- and lower-ionization oxygen lines, constrain the total oxygen column densities of the X-ray absorbers and, modulo their metallicity (which we assume to be $Z_\odot$ in the fit), also their equivalent H column densities.

Finally, we use our hybrid-ionization models[17] to derive ionization fractions of H I, O VI and O VII in a given temperature interval and for a gas volume density of $n_e = 10^{-5}$ cm^{-3} (at densities $n_e > 10^{-4}$ cm^{-3}, photoionization plays a negligible role, and the gas is virtually in collisional ionization equilibrium, whereas for $n_e \lesssim 10^{-4}$ cm^{-3} the uncertainties in the ionization fractions of H I, O VI and O VII

are dominated by the uncertainties on the temperature of the absorber rather than its volume density).

HST-COS spectrum of 1ES 1553+113. 1ES 1553+113 was first observed with the HST-COS on 22 September 2009 for 3.1 ks and 3.8 ks, using the G130M ($\lambda = 1,135-1,480$ Å) and G160M ($\lambda = 1,400-1,795$ Å) gratings, respectively. This spectrum has a signal-to-noise ratio per $\Delta\lambda \approx 0.08$ Å resolution element of SNRE ≈ 23. This observation was published in ref. [20], which reported the detection of 42 intervening IGM systems at $z \lesssim 0.4$. A second spectrum was collected almost two years later, on 24 July 2011, with exposures of 6.4 ks (G130) and 8 ks (G160), which almost doubled the SNRE of the 2009 spectrum over its entire G130M+G160M bandpass.

Here we present a targeted analysis of the full HST-COS spectrum of 1ES 1553+113, aimed at searching specifically for H I or O VI counterparts to the two intervening O VII absorbers identified in the XMM-Newton RGS spectra. We do this by using the fitting package Sherpa of the Chandra Interactive Analysis of Observation (CIAO) software to model the normalized HST-COS spectrum with negative Gaussian functions. When lines are seen in the HST-COS spectrum, we leave all the Gaussian parameters (namely, position, width and normalization factor, or EW) free to vary in the fit and let the fitting routine find the best-fitting parameters by minimizing the statistics with the method *moncar*, which is included in Sherpa. When more than one transition from the same ion is present and the association is secure, we model the absorption lines by linking their relative positions and widths to the relative rest-frame positions. When lines are not seen, but an EW upper limit is needed for a line with position and width bounded by physically motivated limits (that is, the redshifts of the two intervening X-ray systems for the line positions, or their temperatures for the line widths), we set these limits as the minimum and maximum values of the Gaussian position and width during the fit, and let the fitting routine find the best-fitting Gaussian normalization within these limits. We then compute the 3σ upper limit on the normalization of such best-fitting Gaussian by using the Sherpa task *conf*.

When resolved lines of H I are available, we use the empirical correction of ref. [21] ($b_{HI}^{th} = \sqrt{2kT/m_p}$ and $b_{HI}^{th} \approx b_{HI}^{obs}/1.2$, where b_{HI}^{th} and b_{HI}^{obs} are the thermal and observed Doppler parameter, respectively, k is the Boltzmann constant and m_p is the proton mass) to derive the temperature of the FUV gas. Analogously, we use the inverse relationship to set boundary conditions to the width of a H I (or O VI, by factoring in the O/H mass factor) line, when evaluating the 3σ upper limit on the EW of such a line.

Following ref. [22], we derive the ion column densities of FUV lines by running curve-of-growth analyses of the measured line EWs. When more than two transitions from the same ion are present, we check for common solutions in the ion column density versus the Doppler parameter plane (for example, Lyα and Lyβ lines near System 2; see 'H I and O VI counterparts of X-ray systems 1 and 2') and then use the estimated temperature to further constrain the ion column density.

H I and O VI counterparts of X-ray systems 1 and 2. The H I Lyα counterpart to the X-ray System 1 falls just on the long-wavelength side of the strong Ni II ($\lambda = 1,741.55$ Å) line from our Galaxy's interstellar medium. This Ni II line was misidentified in ref. [20] as a H I Lyα absorber at $z = 0.43261$. In our re-analysis of the HST-COS spectrum of 1ES 1553+113, we simultaneously fit the six available Ni II lines ($\lambda = 1,317.22$ Å, $\lambda = 1,370.13$ Å, $\lambda = 1,454.84$ Å, $\lambda = 1,709.40$ Å, $\lambda = 1,741.55$ Å and $\lambda = 1,751.9$ Å). We then add a negative Gaussian to the model to search for a H I Lyα absorber at redshifts within $\pm 1\sigma$ from z_1^X and thermal width bounded by the $\pm 1\sigma$ uncertainty on T_1^X. The fitting routine finds a weak (2.3σ) and broad ($b_{HI}^{obs} \approx 220$ kms^{-1}) line (Extended Data Table 1), which we use to set an upper limit on the EW of the H I Lyα associated with System 1. Analogously, we use the boundary position and width conditions imposed by the redshift and temperature of System 1 to set an upper limit to the EW of the O VI ($\lambda = 1,031.93$ Å) line of System 1 (Extended Data Table 1).

In System 2, two H I Lyα (Fig. 2b) and Lyβ (Fig. 2c) absorbers are present at redshifts consistent with that of the O VII Heα absorber (Fig. 2a), $z_{FUV} = 0.35383 \pm 0.00001$ and $z_{FUV} = 0.35642 \pm 0.00001$. However, the H I lines at $z_{FUV} = 0.35642$ are too narrow ($b_{HI}^{th} \approx 32$ kms^{-1}, implying $T \approx 6 \times 10^4$ K)[21] to be even tentatively associated to the O VII-bearing gas. For the broader H I absorber at $z_{FUV} = 0.35383 \pm 0.00001$, we estimate[21] $T_2^{BHI} = (3.5_{-0.7}^{+0.8}) \times 10^5$ K, only marginally (2σ) consistent with the X-ray estimate. By combining the Doppler widths with the observed line EWs, we obtain $N_{HI,2}^{BHI} = (3.7 \pm 0.1) \times 10^{14}$ cm^{-2}, $N_{OVII,2}^{BHI} = (5.2_{-2.0}^{+3.5}) \times 10^{15}$ cm^{-2} and a 3σ upper limit $N_{OVI,2}^{BHI} < 3.5 \times 10^{13}$ cm^{-2}. By factoring in the ionization fractions, we obtain a solid total H column density for the broader H I absorber: $N_{H,2}^{BHI} = (3.2 \pm 1.0) \times 10^{20}$ cm^{-2}. However, the O columns, derived from O VII and O VI, are inconsistent ($>3\sigma$) with each other: $N_{O,2}^{BHI}$ (O VII) $= (7.7_{-3.8}^{+5.7}) \times 10^{15}$ cm^{-2} and $N_{O,2}^{FUV}$ (O VI) $< 0.7 \times 10^{15}$ cm^{-2}. This, together with the X-ray–FUV temperature inconsistency, imply that (in the collisional ionization equilibrium hypothesis that we adopt here) neither of the two strong H I absorbers at redshifts consistent with z_2^X can be physically associated to System 2. Following the same procedure as for System 1, we therefore set 3σ

upper limits to the EWs of the H I Lyα and O VI ($\lambda = 1,031.93$ Å) transitions (Extended Data Table 1).

FUV–X-ray diagnostics: refined temperature and metallicity. We use the upper limits on the EWs of the O VI ($\lambda = 1,031.93$ Å) transition in System 1 and System 2 to refine the allowed O VI ionization fraction intervals, and so the lower boundaries of the allowed temperature intervals. Namely, we estimate an upper limit on the O VI ionization fraction by dividing the FUV-derived O VI column density upper limit by the 1σ lower boundary on the X-ray-derived oxygen column density: $f_{OVI} = N_{OVI}/N_O < N_{OVI}^{FUV}/[N_O^X-(\Delta N_O^X)]$. For System 1 this gives the revised temperature $T_1^X = (0.8-1.6) \times 10^6$ K and ionization fractions $f_1^{HI} = (2.3 \pm 1.0) \times 10^{-7}, f_1^{OVI} = (0.0041 \pm 0.0018)$ and $f_1^{OVII} = (0.811 \pm 0.098)$. For System 2 we obtain a revised temperature $T_2^X = (0.5-1.4) \times 10^6$ K and ionization fractions $f_1^{HI} = (4.0 \pm 2.5) \times 10^{-7}$, $f_1^{OVI} = (0.019 \pm 0.016)$ and $f_1^{OVII} = (0.855 \pm 0.060)$.

We then use these refined ionization corrections and the upper limits on the EWs of the H I Lyα transition to derive 3σ upper limits on the FUV-equivalent H column densities, and so the 3σ lower limits on the metallicity of the systems. We do this by first dividing the 3σ upper limit on the H I column density by the central value of the revised H I ionization fraction, $N_H^{FUV} = N_{HI}^{FUV}/f_{HI}$, and then comparing this with the central value of the X-ray-estimated equivalent H column, $Z/Z_\odot = N_H^X/N_H^{FUV}$. As an upper limit on the mean metallicity of the systems, we instead assume the value $Z_{ICM} = 0.2 Z_\odot$ found in the peripheries (at r_{500}) of the intra-cluster medium[15]. However, it is possible that the metal distribution in the IGM is inhomogeneous, and in particular it has been argued that oxygen absorbers can arise from relatively over-enriched ($Z \approx 0.5 Z_\odot$) regions[12,13]. Should this be the case for one or both of our O VII absorbers, this would affect (by linearly lowering it) our lower limit on the cosmological mass density of baryons in the WHIM (see 'Cosmological mass density').

Cosmological mass density. Following ref. [23], we estimate the cosmological mass density of baryons in the $10^{5.7}$ K $\leq T \leq 10^{6.2}$ K WHIM by using the formula

$$\Omega_b h^2 (10^{5.7} \text{ K} \leq T \leq 10^{6.2} \text{ K}) = \left(\frac{1}{\rho_c}\right)\left(\frac{m_p \sum_i N_H^i}{(1-Y)d}\right)$$

where $(1-Y)$ is the hydrogen mass fraction (whose inverse is taken to be $\sim$1.3), ρ_c is the universe critical density, N_H^i (for $i = 1, 2$) is the estimated equivalent H column density for systems 1 and 2 and d is the available path length, which (after factoring in the reduction of available RGS bandpass due to both Galactic absorption lines and detector cool pixels) is $\Delta z = 0.42$ or $d = 1,528$ Mpc comoving.

Optical data of 1ES 1553+113. We observed the field of 1ES 1553+113 with the OSIRIS camera at the 10-m Gran Telescope Canarias (GTC). We performed a 4×4 mosaic observation centred on 1ES 1553+113 to cover a $30' \times 30'$ field, in the 5 Sloan Digital Sky Survey (SDSS) bands, u', g', r', i' and z'. Our survey is flux-limited to $r' \approx 23.5$ (a factor of four deeper than the available SDSS data), corresponding to an absolute r' magnitude of -18.9 at $z = 0.5$. We reduced the data using IRAF, along with the *gtcmos* package (http://www.inaoep.mx/~ydm/gtcmos/gtcmos.html). We detected galaxies and performed photometry using *SExtractor*. Following ref. [24], we then derived photometric redshifts using *photoraptor* with a combination of the four band colours plus the pivot magnitude in the r' band. Our photometric redshifts have an accuracy of $\Delta z \approx 0.07$ in the interval $z \approx 0.15-0.6$.

The histogram in Extended Data Fig. 5 is built by considering photometrically identified galaxies in cylindrical volumes with a base radius of 0.5 Mpc and a line-of-sight depth of $\Delta z = 0.07$ at each redshift bin. Galaxies circled in yellow and cyan in Extended Data Figs. 6 and 7, respectively, are photometrically identified galaxies in cylindrical volumes with base radii of 0.5 Mpc and 1.75 Mpc and a line-of-sight depth of $\Delta z = 0.07$, centred at the redshifts of System 1 and System 2. According to our photometric redshifts, both System 1 and System 2 sit at the centre of a large concentration of galaxies: (12, 54) and (8, 72) galaxies with $r' > 23.5$ are found in cylindrical volumes with base radii of (0.5, 1.5) Mpc and a line-of-sight depth of $\Delta z = 0.07$ in the redshift bins of System 1 (where only $\sim$(3, 27) are expected[11]) and System 2 (only $\sim$(2, 18) expected[11]), respectively.

We also have a number of spectroscopic redshifts taken with OSIRIS-MOS at GTC and with the GMOS at the Gemini North Telescope. Data have been reduced and analysed with IRAF. Redshifts are present for 44 galaxies in the $5.5' \times 5.5'$ field around 1ES 1553+113 (35 new measurements and 6 from ref. [25]). For System 1, 13 of our photometrically identified galaxies have spectroscopic redshift and for 8 of them the identification is confirmed (that is, redshifts within ± 900 km s^{-1} from the absorber; solid thick circles in Extended Data Fig. 6). For System 2 only 4 of our photometrically identified galaxies have spectroscopic redshifts and only one of these four identifications is confirmed (solid thick circle in Extended Data Fig. 7), at a velocity of $+370$ km s^{-1} from the absorber's redshift.

On the implausibility of intrinsic absorption. Given the proximity of our two systems with the upper limit $z \lesssim 0.48$ that we estimate for the redshift of our target,

we cannot rule out that these absorbers are imprinted by material intrinsic to the blazar environment and outflowing from this environment at speeds not exceeding $\sim 0.05c$–$0.12c$. However, a number of reasons (also discussed for an analogous case in ref. [17], section 7.6.1), make this scenario implausible. Here we review some of these reasons for the specific cases of System 1 and System 2.

Although photoionized outflows are commonly seen in type-1 Seyferts and quasars (the so called 'warm absorbers'; for example, ref. [26] and references therein), these systems are always seen in multiple species (both in the FUV and X-rays) owing to the smoother ion fraction distribution in photoionized versus collisionally ionized gas (compare, for example, the top and bottom panels in Figs. 1 and 2 of ref. [27]). By contrast, our System 1 and System 2are only seen in O VII, suggesting that electron–ion collisions are the main mechanism of ionization of this gas. Moreover, warm absorbers have typical outflow velocities of only few hundreds to few thousands of kilometres per second, whereas even for our System 1 the implied outflow velocity could be as high as 15,000 km s^{-1}. Finally, warm absorbers have equivalent hydrogen column densities in the range $N_H \approx 10^{20}$–10^{23} cm^{-2}, at least an order of magnitude higher than those observed here[26].

Indeed, no such system has ever been confirmed in blazars, and it is exactly the intrinsic featurelessness of their spectra (together with their relatively high X-ray fluxes) that makes blazars particularly suited for IGM-absorption X-ray experiments (for example, ref. [2] and references therein). Early reports of X-ray absorbers in blazars[28,29] have not been confirmed by later, higher-spectral-resolution observations[30-32]. The only absorption lines detected in the high-resolution, high-signal-to-noise-ratio X-ray spectra of about a dozen blazars are either from our own Galaxy's disk or halo[22,33,34] or claims of intergalactic WHIM (see ref. [2] and references therein). The only two exceptions reported are a misidentification of an O VII Heα line at a redshift consistent with that of Mkn 421[17,35], which is instead a Kβ transition of O II from our own Galaxy[22], and a transient O VIII Kα absorber at the redshift of the blazar H 2356-309[36].

The O VIII Kα absorber reported in ref. [36] has an O VIII column two orders of magnitude larger than those reported here for our two O VII absorbers and, perhaps more importantly, it has a transient nature, appearing in only one out of the five consecutive ~ 80 ks Chandra observations of H 2356-309 performed in September 2008. This is not surprising; any gaseous material intrinsic to the AGN environment must experience strong photoionization by the quasar's radiation field, which in X-rays varies on timescales as short as few hundred seconds. Consistently, the ionization degree of warm absorbers is often seen to vary on timescales from few kiloseconds[37] to months[38]. By contrast, no change is seen in our absorbers over the two years between the first and the second half of our observing campaign (see Extended Data Fig. 4 and Extended Data Table 2, where we also report the EWs of the strong Galactic line of N I during the two epochs for comparison), despite the orders-of-magnitude change commonly experienced by the beamed X-ray luminosity of our target[39]. The lack of variability of our O VII absorbers would require electron volume densities of $n_e \lesssim 10^2$ cm^{-3} for these systems—at least two orders of magnitude lower than the lowest limit estimated for warm absorbers[38]. Therefore, an intrinsic AGN outflow origin for our System 1 (and System 2) seems unlikely.

Such low densities are consistent with the disk or moderately extended halo of the blazar's host galaxy. However, in such a case, only our System 1 could be associated to the blazar's host galaxy (whose redshift would then coincide with that of System 1) and strong O I and O II Kα absorbers should also be seen (as in our own Galaxy; for example, ref. [22] and Extended Data Fig. 1), but are not.

We conclude that a much more plausible explanation for our System 1 and System 2 is intervening absorption by diffuse WHIM or the CGM of intervening galaxies.

Ruling out absorption by a thick disk of an intervening galaxy. Our O VII observations for systems 1 and 2 could in principle be due to absorption by highly ionized material in the thick disk or halo of an intervening galaxy with an impact parameter <100 kpc (for the brightest spirals). In this case, the derived equivalent H column densities should not be used as described in 'Cosmological mass density' to derive the cosmological mass density of hot baryons in the Universe. However, there is no $r' > 23.5$ galaxy with confirmed impact parameter <100 kpc from our two absorbers. Moreover, even if small galaxies, fainter than our survey's limit, were present at such small impact parameters, their thick disks or haloes would also contain a large amount of cool matter with high fractions of neutral and mildly ionized metals. Strong O I and O II absorption is seen, for example, at high galactic latitude in our own Galaxy[22], as well as around the disk (galaxy–absorber impact parameters of ~ 6–100 kpc) of external galaxies[40]. In ref. [22], comparison between lines of sight through the disk of our Galaxy and high-galactic-latitude lines of sight shows that a cool ($T \approx 3,000$ K) ionized medium traced by O I and O II absorbers (also seen here in the spectrum of 1ES 1553+113, together with N I; Fig. 1 and Extended Data Fig. 1) fills both the disk and an extended thick disk or halo of our Galaxy.

Thus, if our System 1 and System 2 were analogous to our local O VII absorbers, and this highly ionized gas were confined in the thick disk or halo of small intervening galaxies, this gas would also probably co-exist with much cooler gas and would create both O VII and strong O I and O II absorption lines in the spectrum of 1ES 1553+113, which are not seen.

16. H.E.S.S. Collaboration. The 2012 flare of PG 1553+113 seen with H.E.S.S. and Fermi-LAT. *Astrophys. J.* **802**, 65 (2015).
17. Nicastro, F. et al. Chandra detection of the first X-ray forest along the line of sight to Markarian 421. *Astrophys. J.* **629**, 700–718 (2005).
18. Asplund, M., Grevesse, N., Sauval, A. J. & Scott, P. The chemical composition of the Sun. *Annu. Rev. Astron. Astrophys.* **47**, 481–522 (2009).
19. Yoshida, N., Furlanetto, S. R. & Hernquist, L. The temperature structure of the warm–hot intergalactic medium. *Astrophys. J.* **618**, L91–L94 (2005).
20. Danforth, C. W., Keeney, B. A., Stocke, J. T., Shull, J. M. & Yao, Y. Hubble/COS observations of the Lyα forest toward the BL Lac object 1ES 1553+113. *Astrophys. J.* **720**, 976–986 (2010).
21. Danforth, C. W., Stocke, J. T. & Shull, J. M. Broad H I absorbers as metallicity-independent tracers of the warm–hot intergalactic medium. *Astrophys. J.* **710**, 613–633 (2010).
22. Nicastro, F. et al. X-ray detection of warm ionized matter in the Galactic halo. *Mon. Not. R. Astron. Soc.* **457**, 676–694 (2016).
23. Schaye, J. Model-independent insights into the nature of the Lyα forest and the distribution of matter in the Universe. *Astrophys. J.* **559**, 507–515 (2001).
24. Brescia, M., Cavuoti, S., Longo, G. & De Stefano, V. A catalogue of photometric redshifts for the SDSS-DR9 galaxies. *Astron. Astrophys.* **568**, A126 (2014).
25. Prochaska, J. X., Weiner, B., Chen, H.-W., Cooksey, K. L. & Mulchaey, J. S. Probing the IGM/galaxy connection. IV. The LCO/WFCCD galaxy survey of 20 fields surrounding UV-bright quasars. *Astrophys. J. Suppl. Ser.* **193**, 28 (2011).
26. Reeves, J. N. et al. A high resolution view of the warm absorber in the quasar MR 2251-178. *Astrophys. J.* **776**, 99 (2013).
27. Nicastro, F., Fiore, F., Perola, G. C. & Elvis, M. Ionized absorbers in active galactic nuclei: the role of collisional ionization and time-evolving photoionization. *Astrophys. J.* **512**, 184–196 (1999).
28. Kruper, J. & Canizares, C. R. A sharp X-ray absorption feature in the BL Lac Object PKS 2155-304. *Bull. Am. Astron. Soc.*, **14** 933 (1982).
29. Madejski, G. M., Mushotzky, R. F., Weaver, K. A., Arnaud, K. A. & Urry, C. M. A ubiquitous absorption feature in the X-ray spectra of BL Lacertae objects. *Astrophys. J.* **370**, 198–204 (1991).
30. Nicastro, F. et al. Chandra discovery of a tree in the X-ray forest toward PKS 2155-304: the local filament? *Astrophys. J.* **573**, 157–167 (2002).
31. Fang, T., Sembach, K. R. & Canizares, C. R. Chandra detection of local O VII Heα absorption along the sight line toward 3C 273. *Astrophys. J.* **586**, L49–L52 (2003).
32. Cagnoni, I., Nicastro, F., Maraschi, L., Treves, A. & Tavecchio, F. A view of PKS 2155-304 with XMM-Newton reflection grating spectrometers. *Astrophys. J.* **603**, 449–455 (2004).
33. Bregman, J. N. & Lloyd-Davies, E. J. X-ray absorption from the Milky Way halo and the local group. *Astrophys. J.* **669**, 990–1002 (2007).
34. Nicastro, F., Senatore, F., Krongold, Y., Mathur, S. & Elvis, M. A distant echo of Milky Way central activity closes the Galaxy's baryon census. *Astrophys. J.* **828**, L12 (2016).
35. Rasmussen, A. P. et al. On the putative detection of $z > 0$ X-ray absorption features in the spectrum of Mrk 421. *Astrophys. J.* **656**, 129–138 (2007).
36. Fang, T., Buote, D. A., Humphrey, P. J. & Canizares, C. R. Detection of a transient X-ray absorption line intrinsic to the BL Lacertae object H 2356-309. *Astrophys. J.* **731**, 46 (2011).
37. Krongold, Y. et al. The compact, conical, accretion-disk warm absorber of the Seyfert 1 galaxy NGC 4051 and its implications for IGM-galaxy feedback processes. *Astrophys. J.* **659**, 1022–1039 (2007).
38. Krongold, Y. et al. Suzaku monitoring of the Seyfert 1 galaxy NGC 5548: warm absorber location and its implication for cosmic feedback. *Astrophys. J.* **710**, 360–371 (2010).
39. Ackermann, M. et al. Multiwavelength evidence for quasi-periodic modulation in the gamma-ray blazar PG 1553+113. *Astrophys. J.* **813**, L41 (2015).
40. Lehner, N. et al. The bimodality distribution of the cool circumgalactic medium at z ≲ 1. *Astrophys. J.* **770**, 138 (2013).
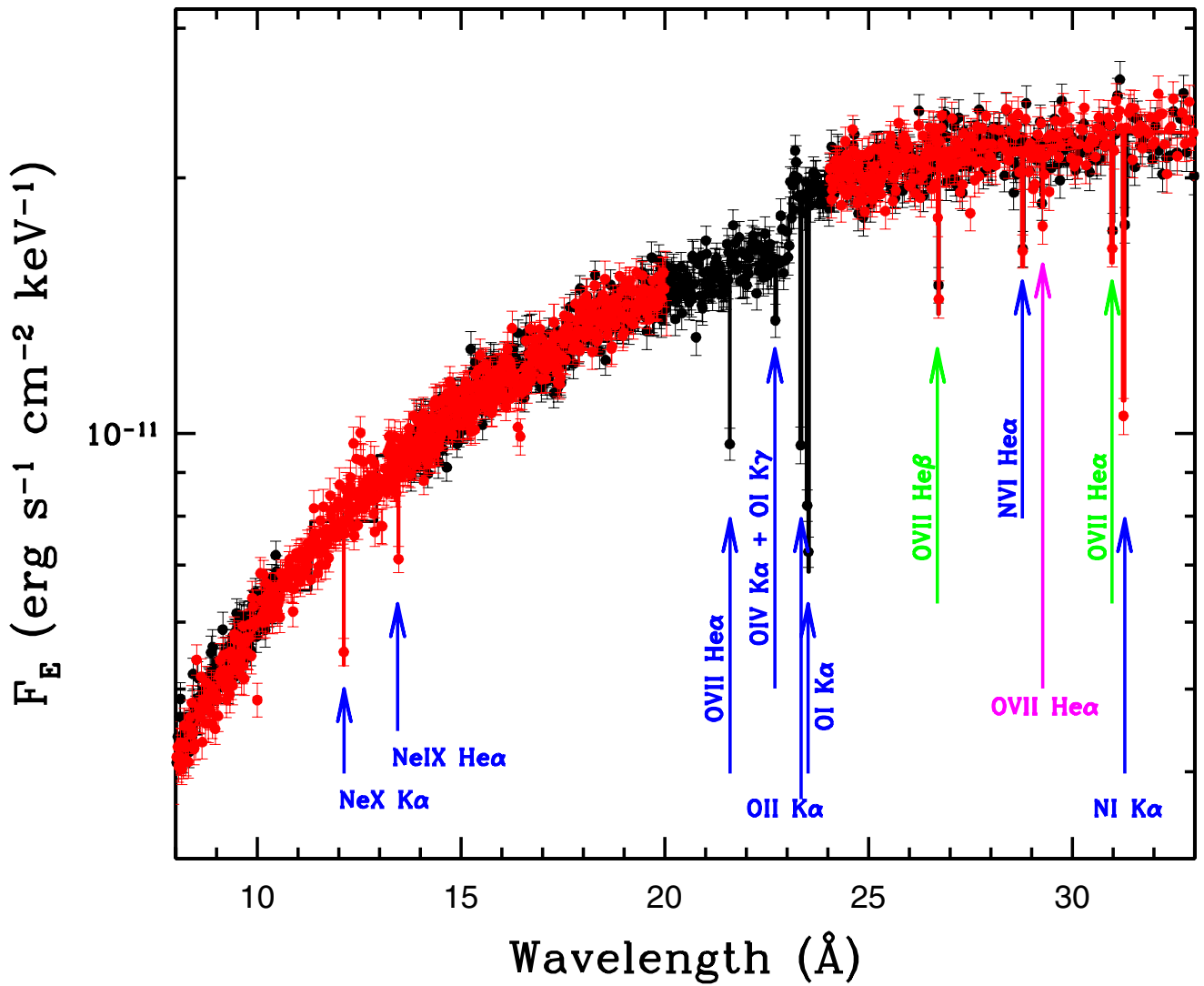
Extended Data Fig. 1 | XMM-Newton RGS spectra of 1ES 1553+113. Broadband, unfolded RGS1 (black points; 1σ error bars) and RGS2 (red points; 1σ error bars) spectra (in bins with a signal-to-noise ratio per bin ≥ 20) and best-fitting models (black and red histograms) for the blazar 1ES 1553+113, in physical units. Blue arrows mark Galactic absorption lines; green and magenta arrows indicate absorption lines from our WHIM System 1 and System 2, respectively. F_E, source flux (power per unit area and energy).
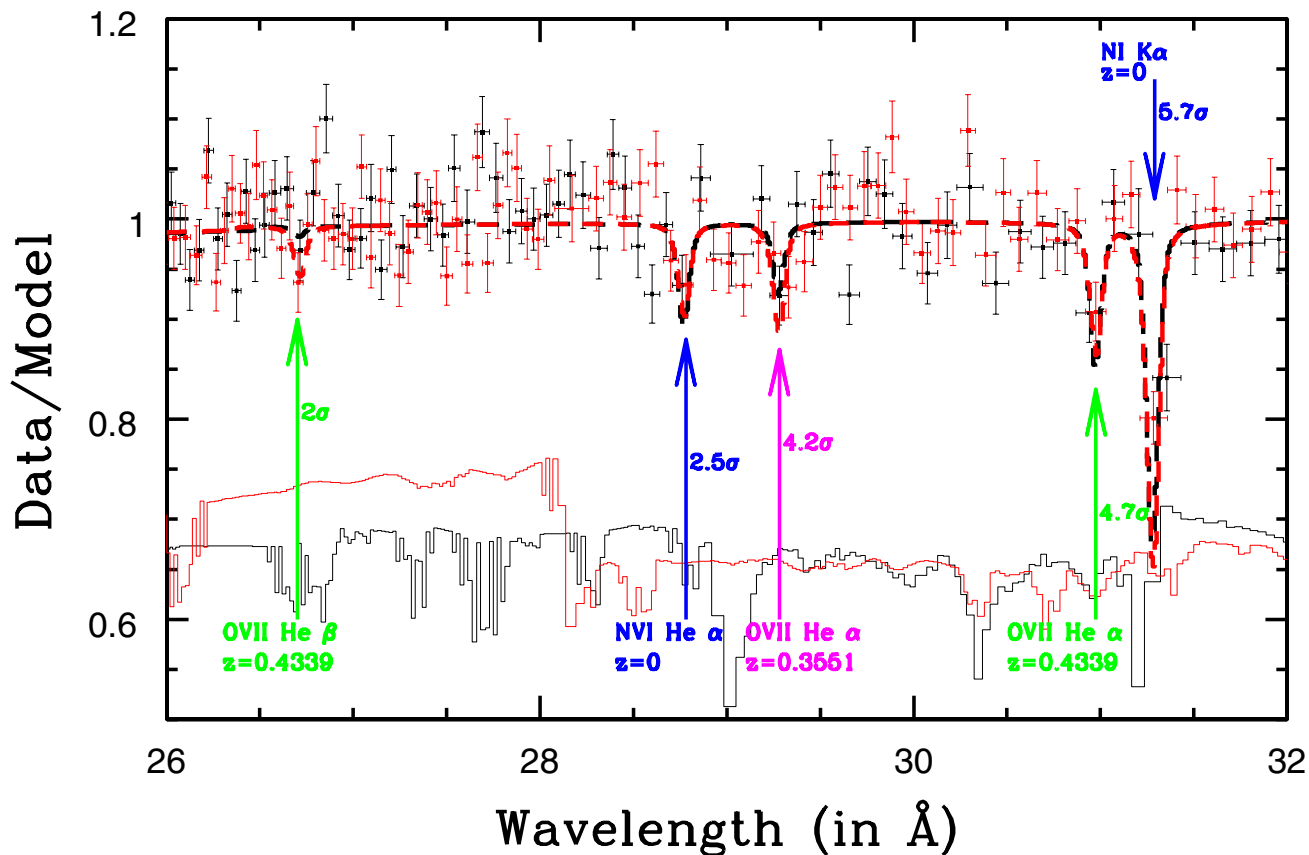
Extended Data Fig. 2 | Normalized XMM-Newton RGS spectra of 1ES 1553+113. Normalized raw RGS1 (black points; 1σ error bars) and RGS2 (red points; 1σ error bars) data (in bins with a signal-to-noise ratio per bin ≥ 30) of the blazar 1ES 1553+113, in the wavelength interval $\lambda = 26-32$ Å. Thick dashed curves are the RGS1 (black) and RGS2 (red) best-fitting models, folded through the response functions of the RGSs.

Thin solid curves at the bottom of the graph are RGS1 (black) and RGS2 (red) effective areas (in arbitrary units), showing instrumental features due to cool pixels in the dispersing detectors. Of the five absorption lines shown, only the weak O VII Heβ at $z^X = 0.4339$, and only in RGS1, can be affected by the presence of an instrumental feature.
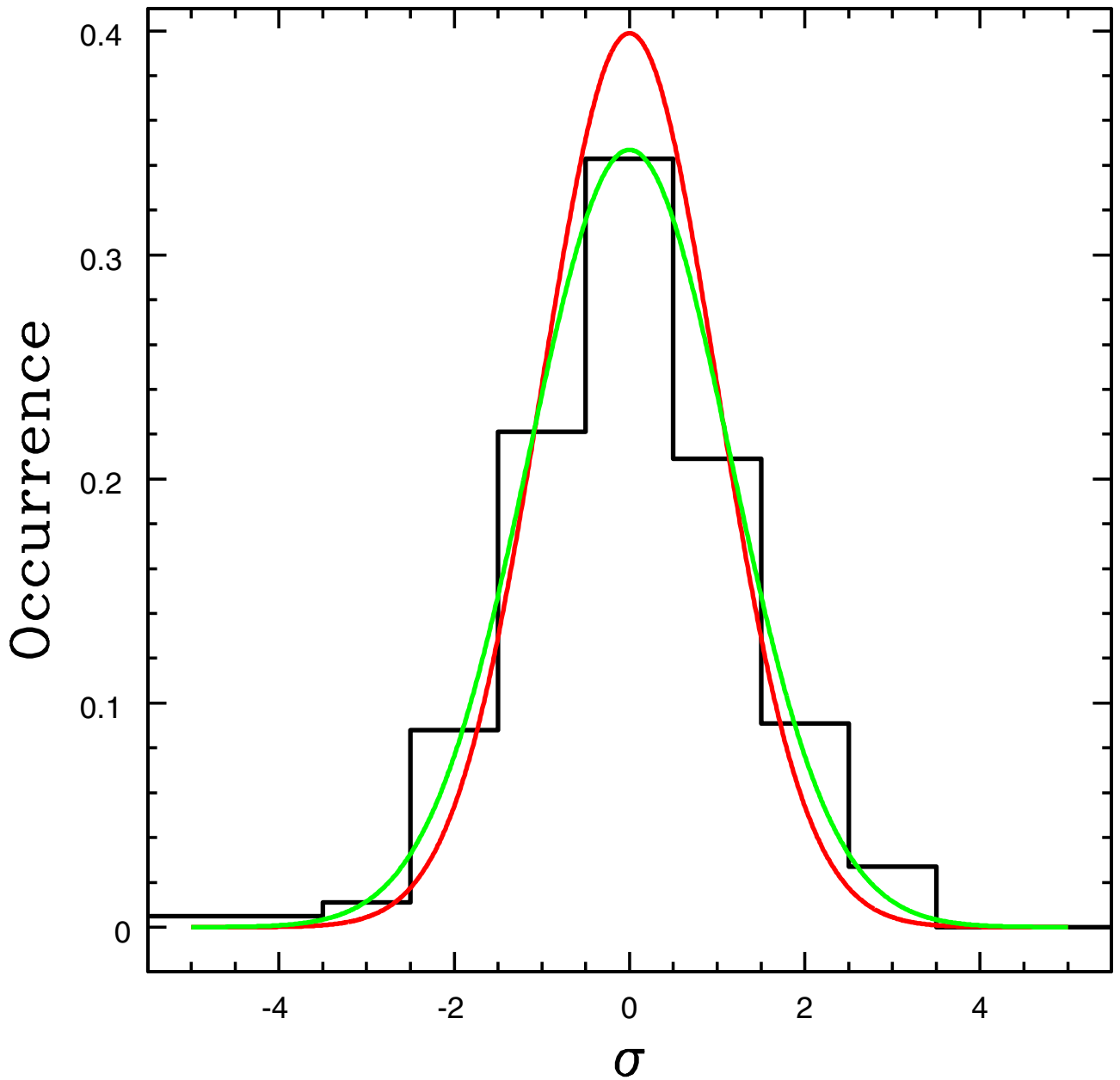
Extended Data Fig. 3 | Assessing systematic errors in the RGS spectrum of 1ES 1553+113. Outcome of a Monte Carlo procedure consisting of 10,000 evaluations of the single-line statistical significance of an unresolved (that is, broadened to the instrument line spread function) Gaussian added to the best-fitting continuum-plus-line model of the RGS spectrum of 1ES 1553+113 (see Methods). At each run, the line position is frozen at a random position in the range 8–33 Å, and its EW is allowed to vary freely from negative (emission) to positive (absorption). The data distribution is symmetric but slightly flatter than the red curve that shows the expected normal distribution for a standard deviation of unity. The normal distribution that best fits our Monte Carlo results has a standard deviation of 1.15 (green curve).
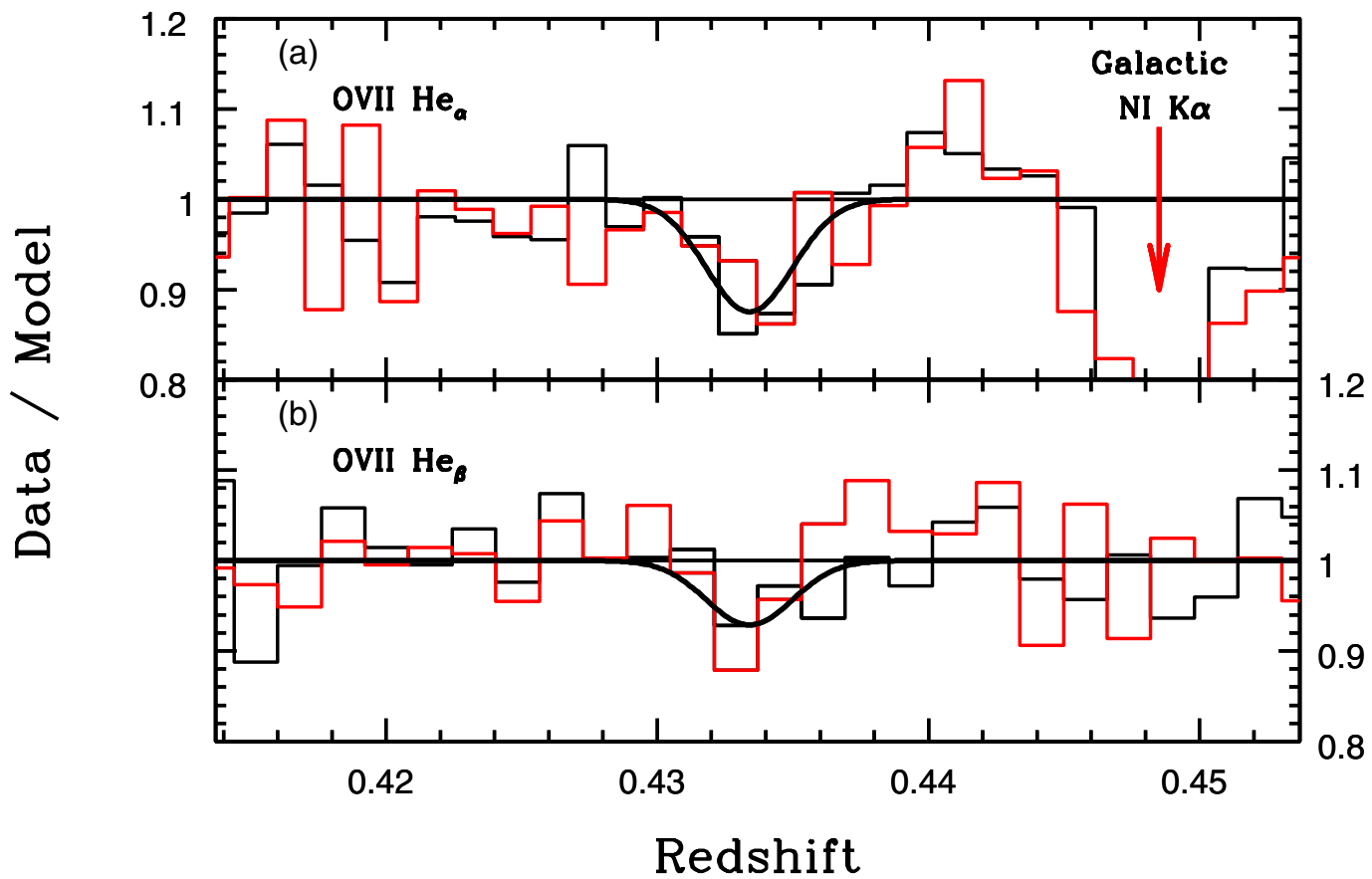
Extended Data Fig. 4 | Constancy of the $z = 0.4339$ O VII absorber.
a, b, RGS spectra of 1ES 1553+113 obtained in the 2015 (black) and 2017 (red) observations for 800 ks and 950 ks, respectively, centred around the O VII Heα (**a**) and Heβ (**b**) transitions of System 1. The two lines are consistent with no variability between the two epochs, within their 1σ errors (Extended Data Table 2).
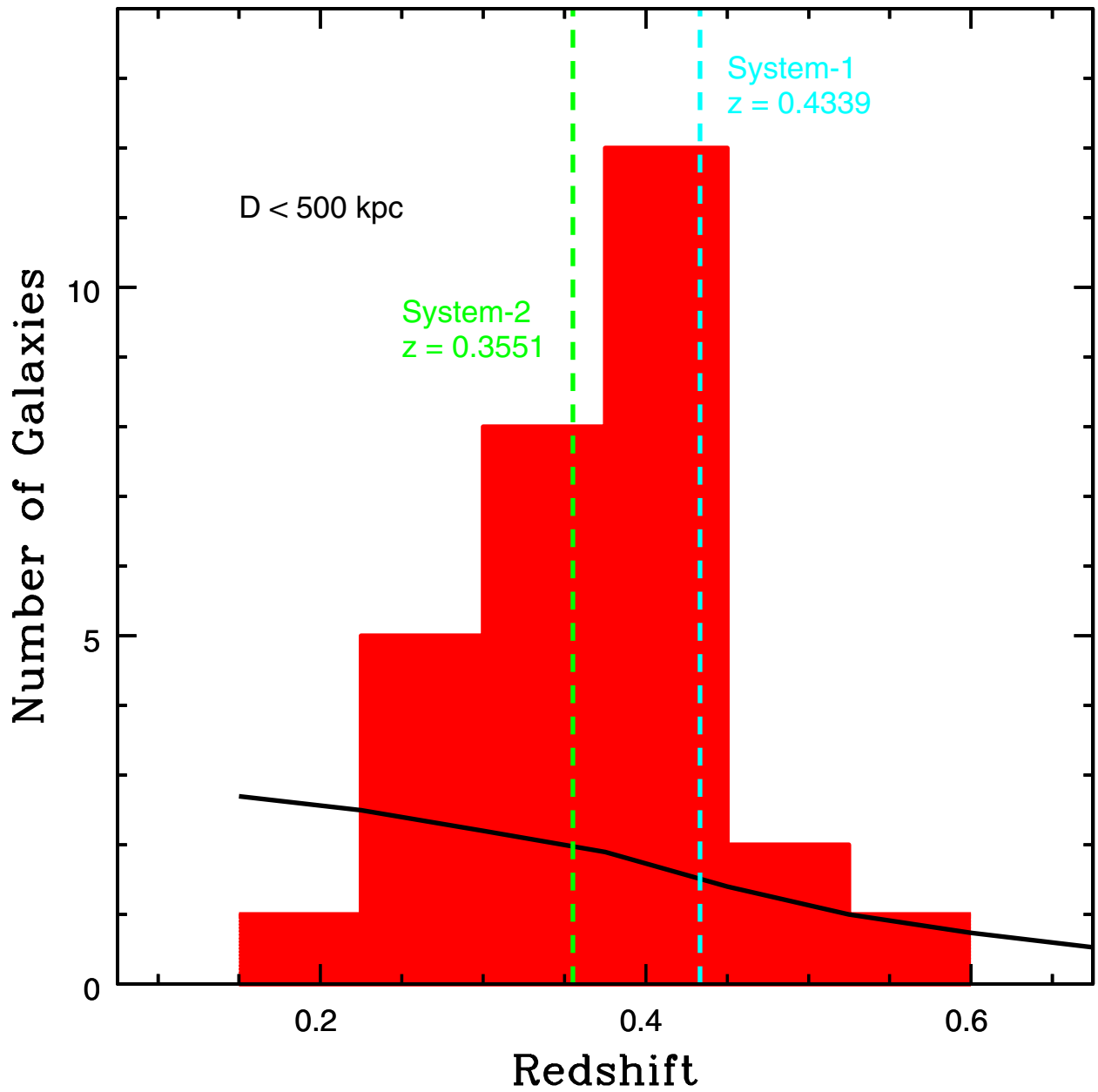
Extended Data Fig. 5 | Galaxy photometric redshifts. Histogram of photometric redshifts of $r' > 23.5$ galaxies within cylindrical volumes with base radii of 500 kpc at each redshift interval and a line-of-sight depth of $\Delta z = 0.075$ (at 1σ redshift accuracy), centred on the line of sight to the blazar 1ES 1553+113. The black curve is the average number of galaxies with $r' > 23.5$ expected within the explored volumes at each redshift bin, based on the galaxy $\log N$–$\log S$ from ref. [11] (where N is the number of galaxies with surface brightness $\geq S$ and we use a common but conservative $B - r' = 1$ for all galaxy types, where B is the galaxy's B magnitude). Vertical dashed green and blue lines indicate the redshifts of System 1 and System 2, respectively.
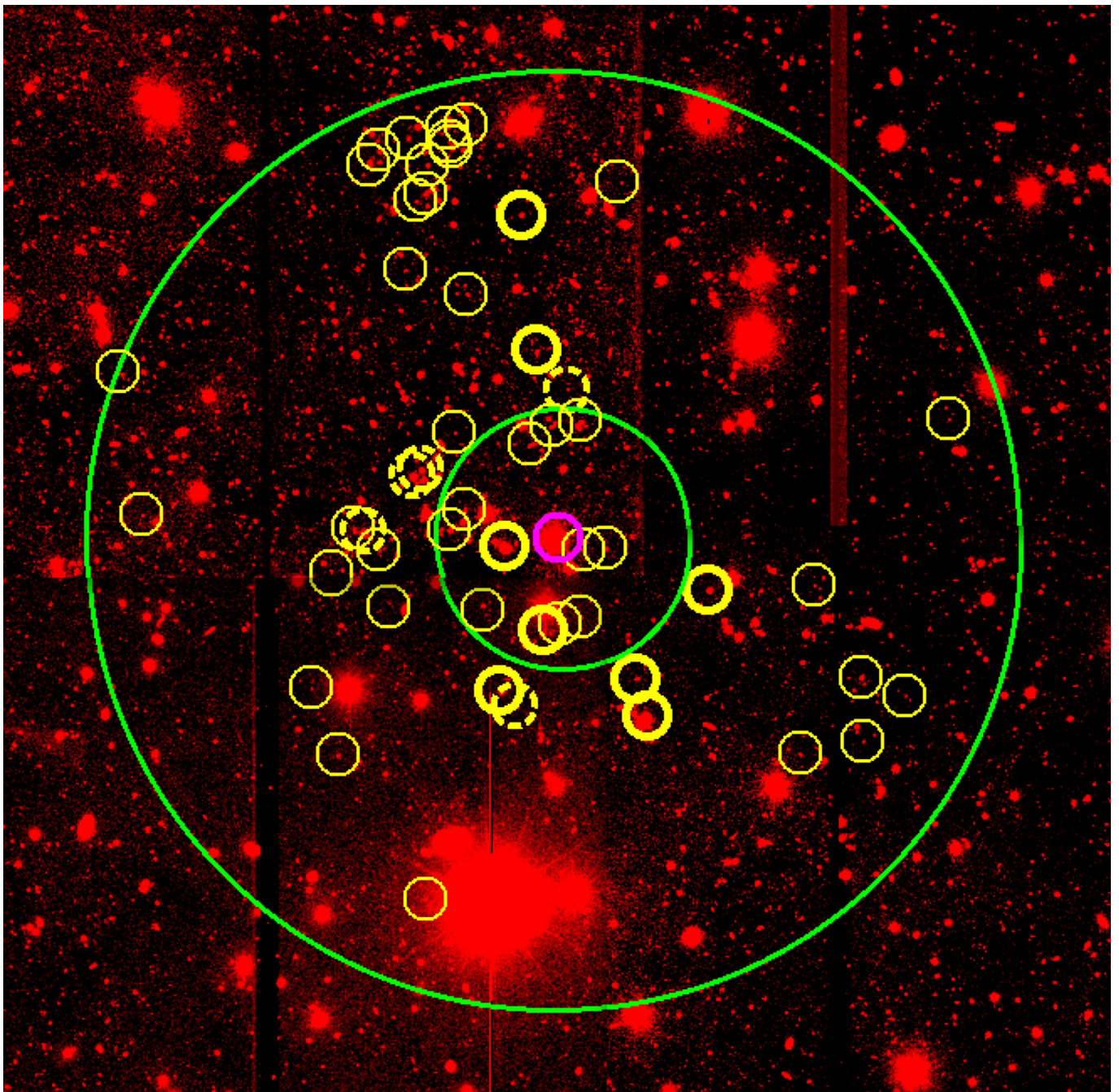
Extended Data Fig. 6 | $r' > 23.5$ galaxies surrounding WHIM System 1.
OSIRIS-GTC mosaic (in band r') of the $12' \times 12'$ field surrounding the
line of sight to 1ES 1553+113 (indicated by the magenta circle). Green
circles have radii of 500 kpc and 1.75 Mpc at $z = 0.4125$. Thin yellow circles
highlight the positions of galaxies with photometric redshift estimates
within the $z = 0.375$–0.450 interval, whereas thicker circles highlight
spectroscopic redshifts (solid, confirmed; dashed, unconfirmed).
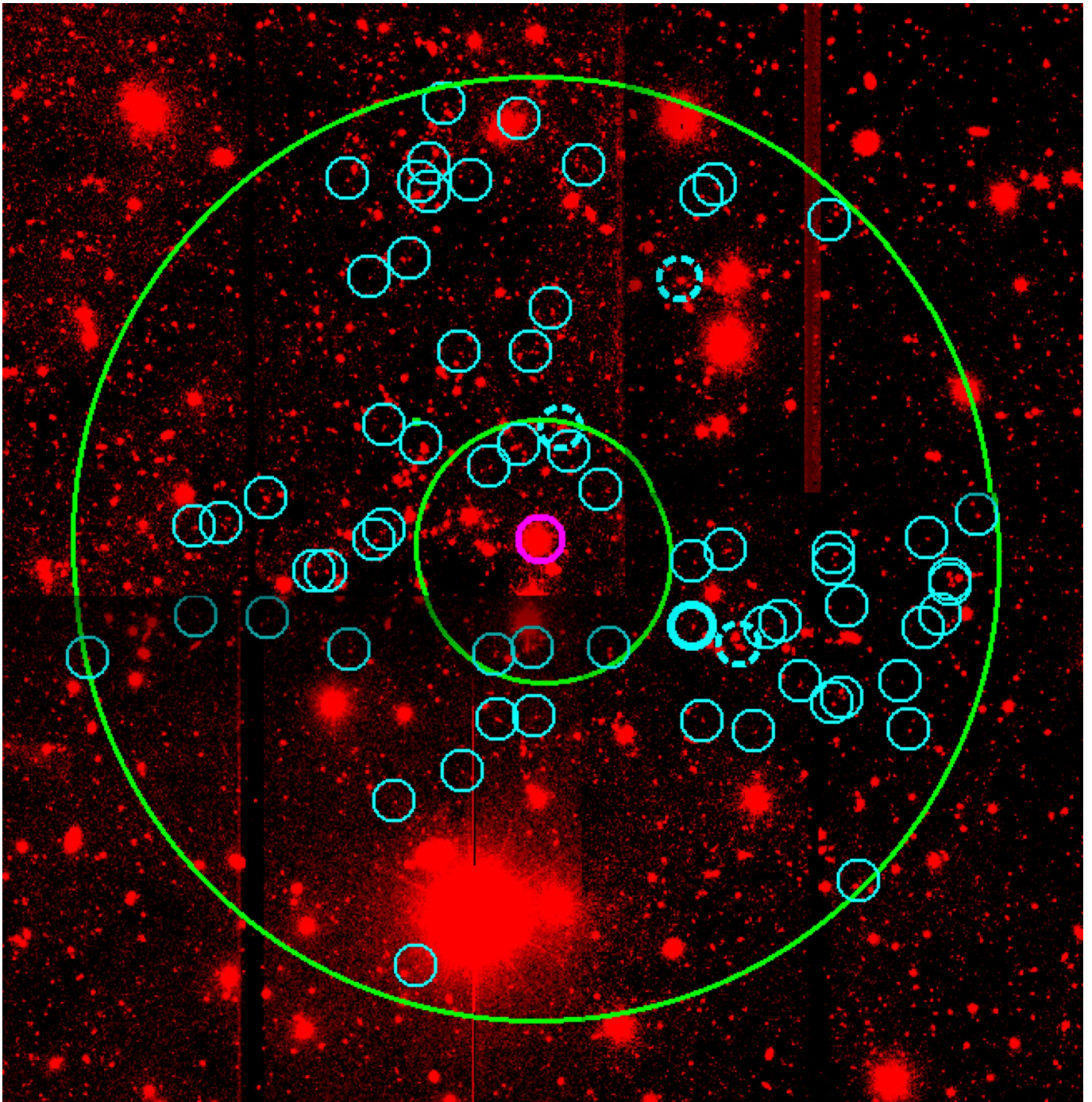
Extended Data Fig. 7 | r′ > 23.5 galaxies surrounding WHIM System 2. Same as Extended Data Fig. 5, but for System 2, in the $z = 0.300$–0.375 interval.

Extended Data Table 1 | Absorption lines of System 1 and System 2

Wavelength (Å)	Id	Redshift	b (km s^{-1})	EW$_{obs}$ (mÅ)	Significance (σ)
30.975±0.017	OVII He-α	0.4339±0.0008	NA	14.7±3.1	4.1−4.7
26.69±0.09	OVII He-β	0.4326±0.0048	NA	$4.4^{+2.7}_{-2.2}$	1.7−2.0
1742.18−1744.24	HI Ly-α	0.4331-0.4347	90−220	<110	3.0u.l.
1478.86−1480.51	OVI 2s2p$_{1/2}$	0.4331-0.4347	55-128	<30	3.0 u.l.
$29.27^{+0.01}_{-0.03}$	OVII He-α	$0.3551^{+0.0003}_{-0.0015}$	NA	$10.5^{+2.9}_{-2.5}$	3.7−4.2
1645.53−1647.72	HI Ly-α	0.3536−0.3554	96−190	<98	3.0 u.l.
1396.82−1398.68	OVI 2s2p$_{1/2}$	0.3536−0.3554	57−113	<49	3.0 u.l.

Id, identification; u.l., upper limit; EW$_{obs}$, observed EW.

Epoch	Transition	System	EW$_{obs}$ (in mÅ)
1	OVII He-α	1	17±5
2	OVII He-α	1	15±5
1	OVII He-β	1	7±4
2	OVII He-β	1	8±3
1	OVII He-α	2	8±5
2	OVII He-α	2	12±4
1	NI Kα	Gal	39±7
2	NI Kα	Gal	37±6

Gal, Galactic.

System	T (10^6 K)	N_0 $(10^{15} \text{ cm}^{-2})$	$N_H(Z/Z_\odot)^{-1}$ $(10^{19} \text{ cm}^{-2})$	Z $(Z_\odot)$
1	1.2 ± 0.4	$7.8^{+3.9}_{-2.4}$	$1.6^{+0.8}_{-0.5}$	≥ 0.1
2	0.95 ± 0.45	$4.4^{+2.4}_{-2.0}$	$0.9^{+0.5}_{-0.4}$	≥ 0.1